IODP-ICDP Expedition 364 Scientists:

S. P. S. Gulick, Institute for Geophysics and Department of Geological Sciences, Jackson School of Geosciences, University of Texas at Austin, Austin, TX, USA
J. V. Morgan, Department of Earth Science and Engineering, Imperial College London, London, UK
T. J. Bralower, Department of Geosciences, Pennsylvania State University, State College, PA, USA E. Cheno, Géosciences Montpellier, Université de Montpellier, Montpellier, France
G. L. Christeson, Institute for Geophysics, Jackson School of Geosciences, University of Texas at Austin, Austin, TX, USA,
P. Claeys, Analytical, Environmental and GeoChemistry, Vrije Universiteit Brussel, Brussels, Belgium
C. S. Cockell, Centre for Astrobiology, School of Physics and Astronomy, University of Edinburgh, Edinburgh, UK
M. J. L. Coolen, Department of Chemistry, WA Organic and Isotope Geochemistry Centre, Curtin University, Perth, Western Australia, Australia
L. Ferrière, Natural History Museum, Vienna, Austria
C. Gebhardt, Alfred Wegener Institute Helmholtz Centre of Polar and Marine Research, Bremerhaven, Germany
K. Goto, International Research Institute of Disaster Science, Tohoku University, Sendai, Japan, now at: Department of Earth and Planetary Science, University of Tokyo, Japan
S. Green, British Geological Survey, Edinburgh, UK
H. Jones, Department of Geosciences, Pennsylvania State University, University Park, PA, USA
D. A. Kring, Lunar and Planetary Institute, Houston, TX, USA
E. LeBer, School of Geography, Geology, and the Environment, University of Leicester, Leicester, UK
J. Lofi, Géosciences Montpellier, Université de Montpellier, Montpellier, France
C. M. Lowery, Institute for Geophysics, Jackson School of Geosciences, University of Texas at Austin, Austin, TX, USA
R. OcampoTorres, Groupe de Physico Chimie de l'Atmosphère, L'Institut de Chimie et Procédés pour l'Énergie, l'Environnement et la Santé (ICPEES), Université de Strasbourg, Strasbourg, France
L. Perez Cruz, Instituto de Geofísica, Universidad Nacional Autónoma De México, Mexico, Mexico
A. E. Pickersgill, School of Geographical and Earth Sciences, University of Glasgow, Glasgow, now at: Argon Isotope Facility, Scottish Universities Environmental Research Centre, East Kilbride, UK
M. H. Poelchau, Institut für Geound Umweltnaturwissenschaften, Albert Ludwigs Universität, Freiburg, Germany
A. S. P. Rae, Department of Earth Science and Engineering, Imperial College London, London, UK, now at: Institut für Geound Umweltnaturwissenschaften, Albert Ludwigs Universität, Freiburg, Germany
C. Rasmussen, Institute for Geophysics, Jackson School of Geosciences, University of Texas at Austin, Austin, TX, USA, Department of Geology and Geophysics, University of Utah, Salt Lake City, UT, USA
M. Rebolledo Vieyra, Independent consultant, Cancun, Mexico
U. Riller, Institut für Geologie, Universität Hamburg, Hamburg, Germany
H. Sato, Japan Agency for Marine Earth Science and Technology, Kanagawa, Japan
D. Schmitt, Department of Earth, Atmospheric, and Planetary Sciences, Purdue University, West Lafayette, IN, USA
J. Smit, Faculty of Earth and Life Sciences (FALW), Vrije Universiteit Amsterdam, Amsterdam, Netherlands
S. M. Tikoo, Earth and Planetary Sciences, Rutgers University, New Brunswick, NJ, USA, now at: Department of Geophysics, Stanford University, Stanford, California USA
N. Tomioka, Kochi Institute for Core Sample Research, Japan Agency for Marine Earth Science and Technology, Kochi, Japan
J. Urrutia Fucugauchi, Instituto de Geofísica, Universidad Nacional Autónoma De México, Mexico, Mexico
M. T. Whalen, Department of Geosciences, University of Alaska Fairbanks, Fairbanks, AK, USA
A. Wittmann, Eyring Materials Center, Arizona State University, Tempe, AZ, USA
L. Xiao, School of Earth Sciences, Planetary Science Institute, China University of Geosciences, Wuhan, China
K. E. Yamaguchi, Department of Chemistry, Toho University, Chiba, Japan, now at: Disaster Prevention Research Institute, Kyoto University, Kyoto, Japan

Supplemental Information Appendix Figure Captions

Figure S1. Bulk major elemental compositions of the upper peak ring interval of the IODP-ICDP 364 core determined by μXRF together with μXRF maps of representative samples covering the suevite stratigraphy.

Figure S2. Sulfur weight percentages in the upper peak ring interval of the IODP-ICDP 364 core, determined by two independent measurement techniques and showing values consistently lower than 0.7 wt % S. The grey shading represents the limit of detection of S.

Figure S3. μXRF map of a polished thick section from the uppermost suevite unit showing a multi-elemental distribution map for Fe, Si, Ca, and S and single-elemental heatmap for S. The presence of both Fe and S in the crystals in the upper right corner of the slab clearly demonstrates that the enriched S content in this level is caused by the presence of iron sulfide, which has petrographically been confirmed to be pyrite (FeS2).

Figure S4. Example of classification step of machine learning pipeline completed on the M0077 impactite cores (width of cores shown are 86 mm). A) Training data used to classify core section 72-2 where impact melt rock is gray, carbonates are blue, siltstone and cherts are green, basement types are red, and matrix types are pink and orange. B) High-resolution linescan image of core. C) DeepFeature classification results on this core section.

Figure S5. Cylinder unwrap images from X-ray CT volume with 0.3 mm resolution showing representative sections of suevite and impact melt rock. All depths are in mCCSF-A (vertically stacked images ignoring core overlaps). A) Upper suevite within higher energy deposits in Unit 2A. B) Middle suevite showing low CT number matrix (carbonate) and size sorting in Unit 2B. C) Lower suevite unsorted with mixed low and higher CT number matrix (melt rock) in Unit 2B. D) Impact melt rock with clasts visible in Unit 3B.

Figure S6. Point counting of each recovered core from Unit 2 (Upper Peak Ring, suevite) at Site M0077 reported as percent matrix and clasts.

Figure S7: Paleomagnetic and high temperature magnetic susceptibility results for upper peak ring impactites. A) Magnetic inclination versus depth for characteristic magnetization components in peak ring impactites. Lithologic units are labeled using red text and boundaries. The expected magnetic inclination at the time of impact (-46 degrees) is shown with a vertical blue dashed line. B) High-temperature magnetic susceptibility measurements with inferred Curie temperature labeled for representative magnetite-bearing suevite sample 364-M0077-62A-2-W-55.0-57.5 cm, 683.04 mbsf. Warming curve is shown in red and cooling curve is shown in blue.

Figure S8. Example of 25 fields of view, ~62500 square microns, from Core 40 Section 1 at 103.5 cm (617.27 mbsf). Estimate of number of charcoal fragments at this depth by area was 1220 (see Methods).

Figure S9: Flooding timescale of the Chicxulub crater for different estimates of the water depth in the preimpact basin to the north-northeast of the Chicxulub crater. For water depths exceeding 1 km, flooding to a level that would inundate the peak ring, which stood ~500 m above the crater floor, is expected to take as little as 30-minutes to one hour. The one-dimensional flooding model assumes a unidirectional ingress of water from the north-northwest that is reflected off the inside of the crater rim on the southern side. The approximation neglects various factors that might delay the resurge, such as drag as the water surges over the crater floor and interactions between the flood water and the hot melt sheet, which might vaporize some of the water and generate MWI products.

Figure S10. Polyaromatic hydrocarbon data expressed as ratios of perylene to benzo(a)pyrene and benzo(e)pyrene. These data amplify the observation of terrestrial input to the crater correlated with the uppermost high-energy deposit within Unit 2A.

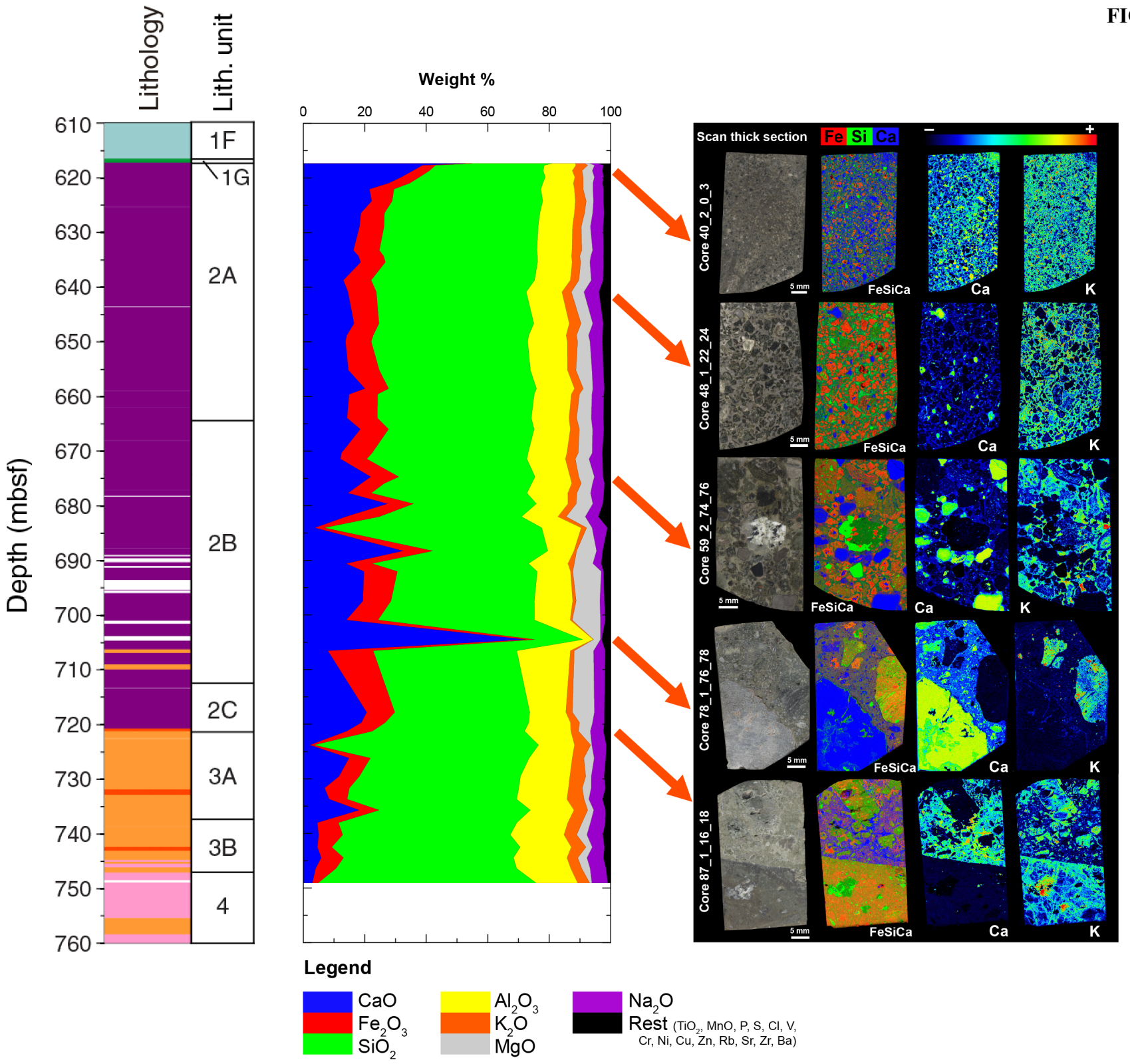
Lithology
Lith. unit
Depth (mbsf)
610
620
630
640
650
660
670
680
690
700
710
720
730
740
750
760
1F
1G
2A
2B
2C
3A
3B
4
Weight %
0
20
40
60
80
100
Scan thick section
Fe
Si
Ca
Core 40_2_0_3
Core 48_1_22_24
Core 59_2_74_76
Core 78_1_76_78
Core 87_1_16_18
5 mm
FeSiCa
Ca
K
Legend
CaO
Fe2O3
SiO2
Al2O3
K2O
MgO
Na2O
Rest (TiO2, MnO, P, S, Cl, V, Cr, Ni, Cu, Zn, Rb, Sr, Zr, Ba)

FIGURE S2

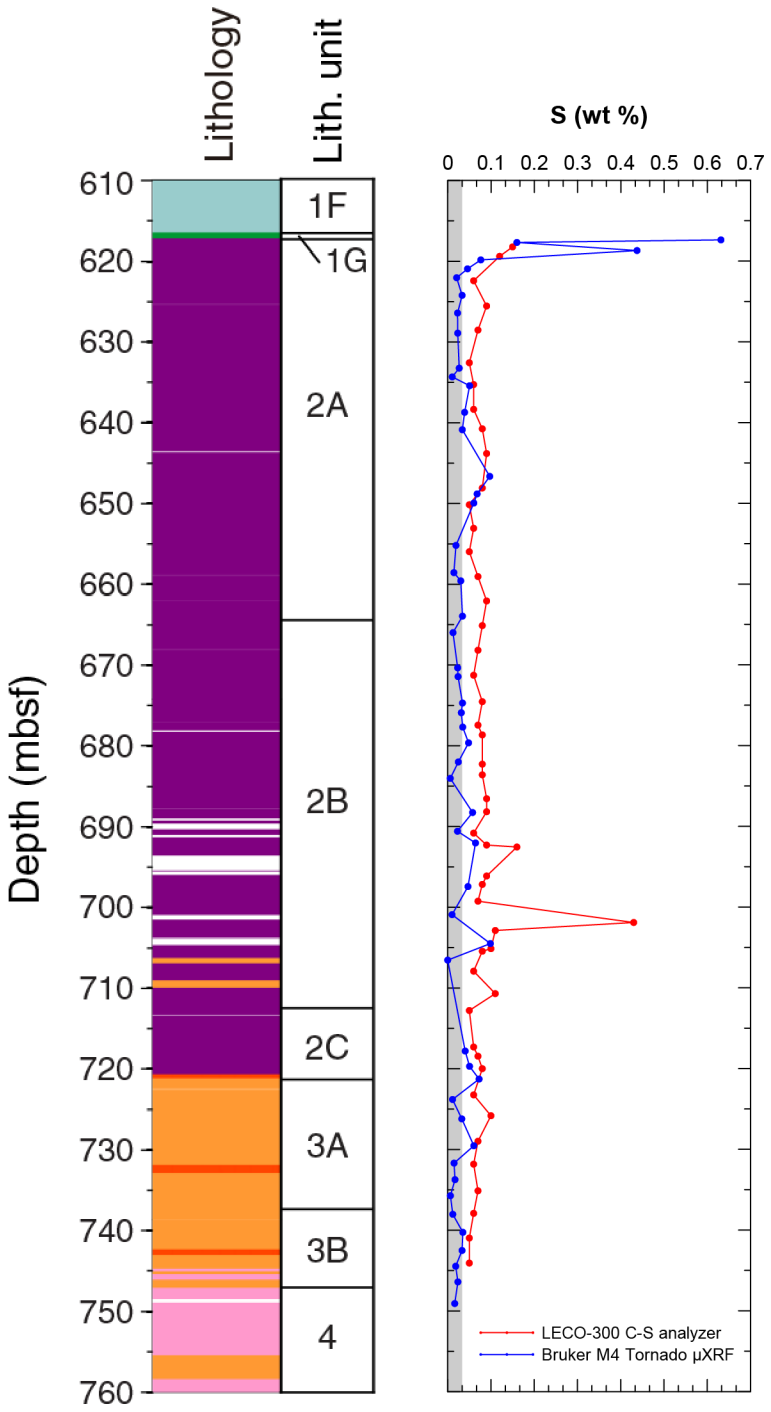
Lithology
Lith. unit
Depth (mbsf)
610
620
630
640
650
660
670
680
690
700
710
720
730
740
750
760
1F
1G
2A
2B
2C
3A
3B
4
S (wt %)
0
0.1
0.2
0.3
0.4
0.5
0.6
0.7
LECO-300 C-S analyzer
Bruker M4 Tornado µXRF

FIGURE S3

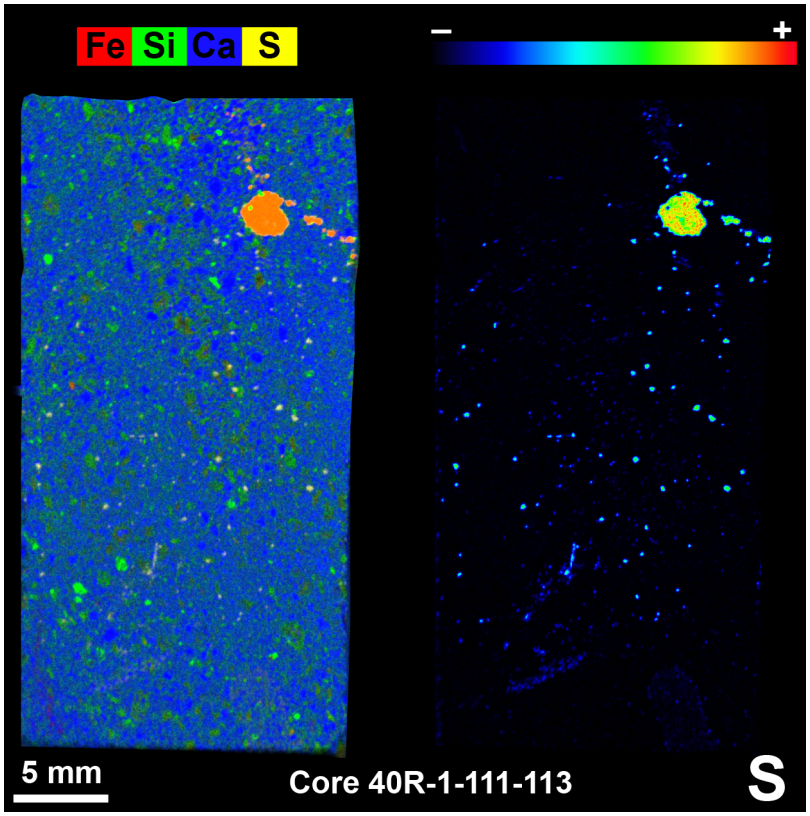

FIGURE S4

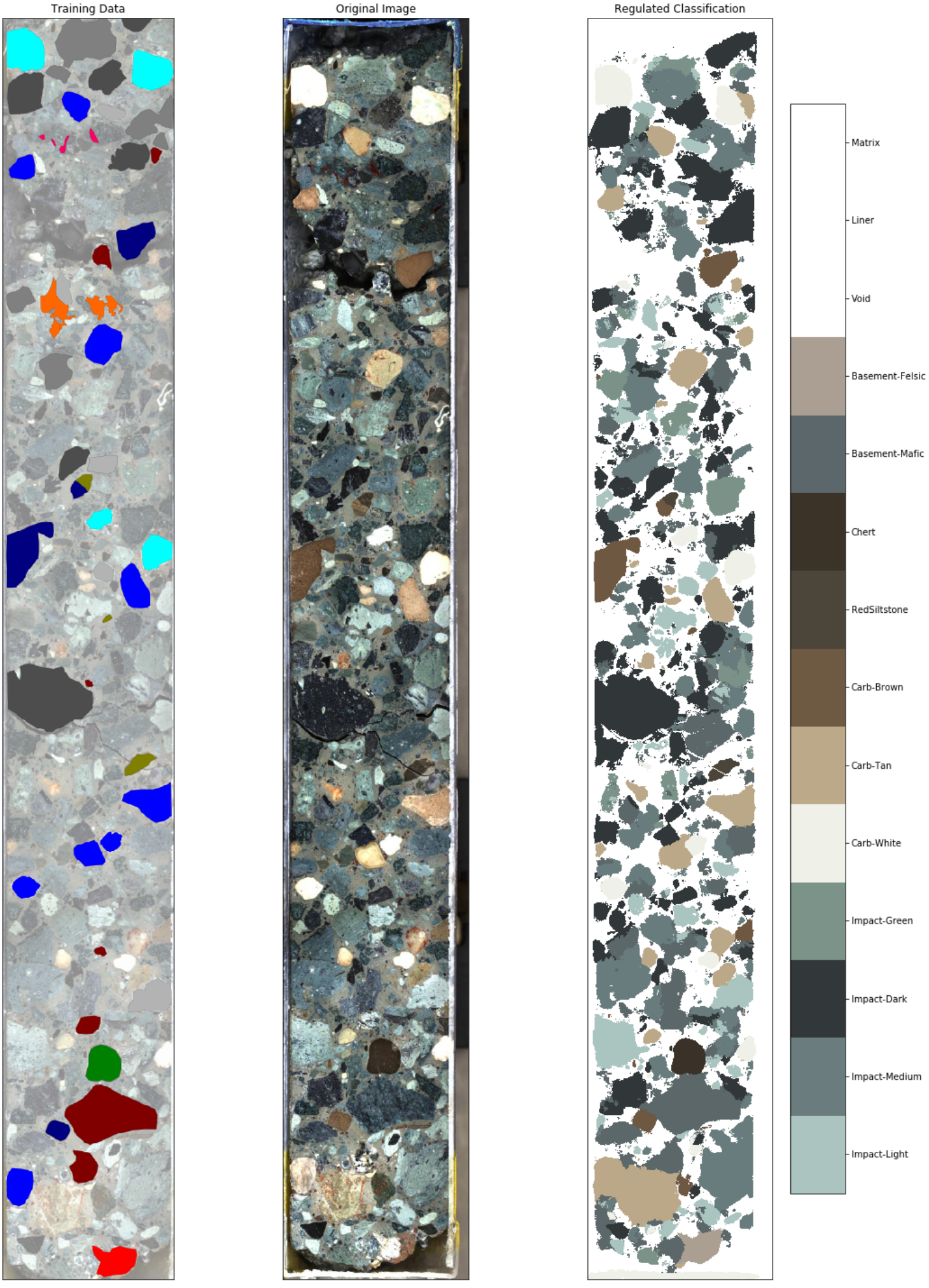
Training Data
Original Image
Regulated Classification
Matrix
Liner
Void
Basement-Felsic
Basement-Mafic
Chert
RedSiltstone
Carb-Brown
Carb-Tan
Carb-White
Impact-Green
Impact-Dark
Impact-Medium
Impact-Light

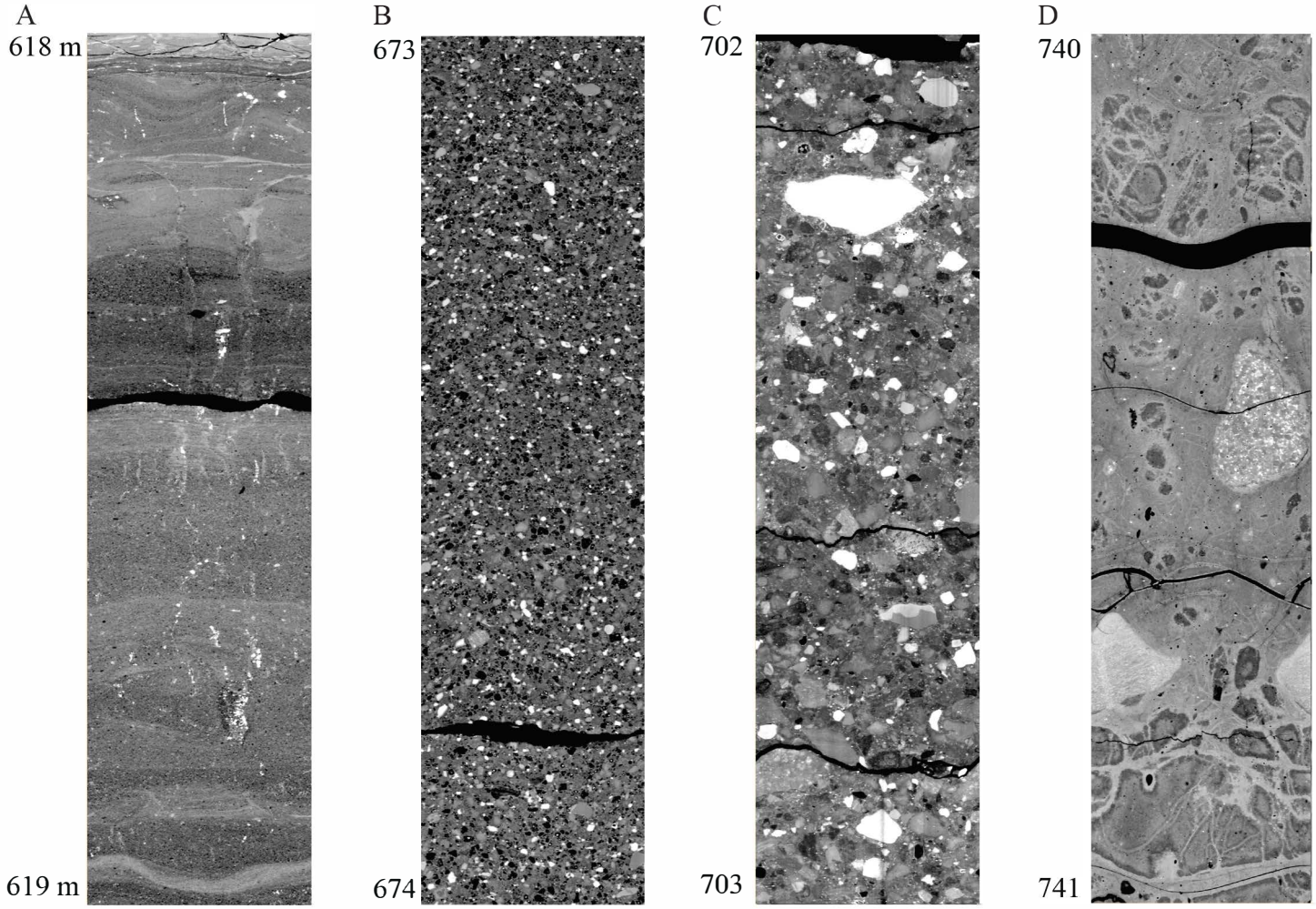
A
618 m
619 m
B
673
674
C
702
703
D
740
741

FIGURE S6

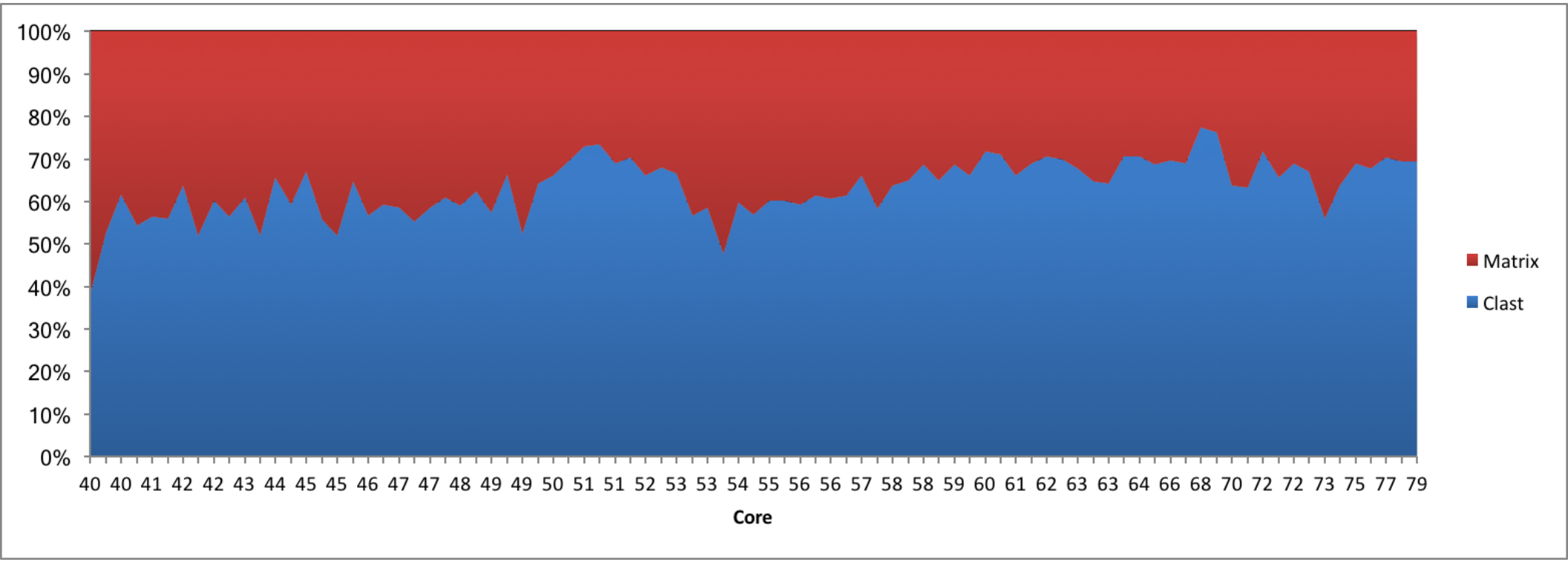
100%
90%
80%
70%
60%
50%
40%
30%
20%
10%
0%
40 40 41 42 42 43 44 45 45 46 47 47 48 49 49 50 51 51 52 53 53 54 55 56 56 57 58 58 59 60 61 62 63 63 64 66 68 70 72 72 73 75 77 79
Core
Matrix
Clast

FIGURE S7

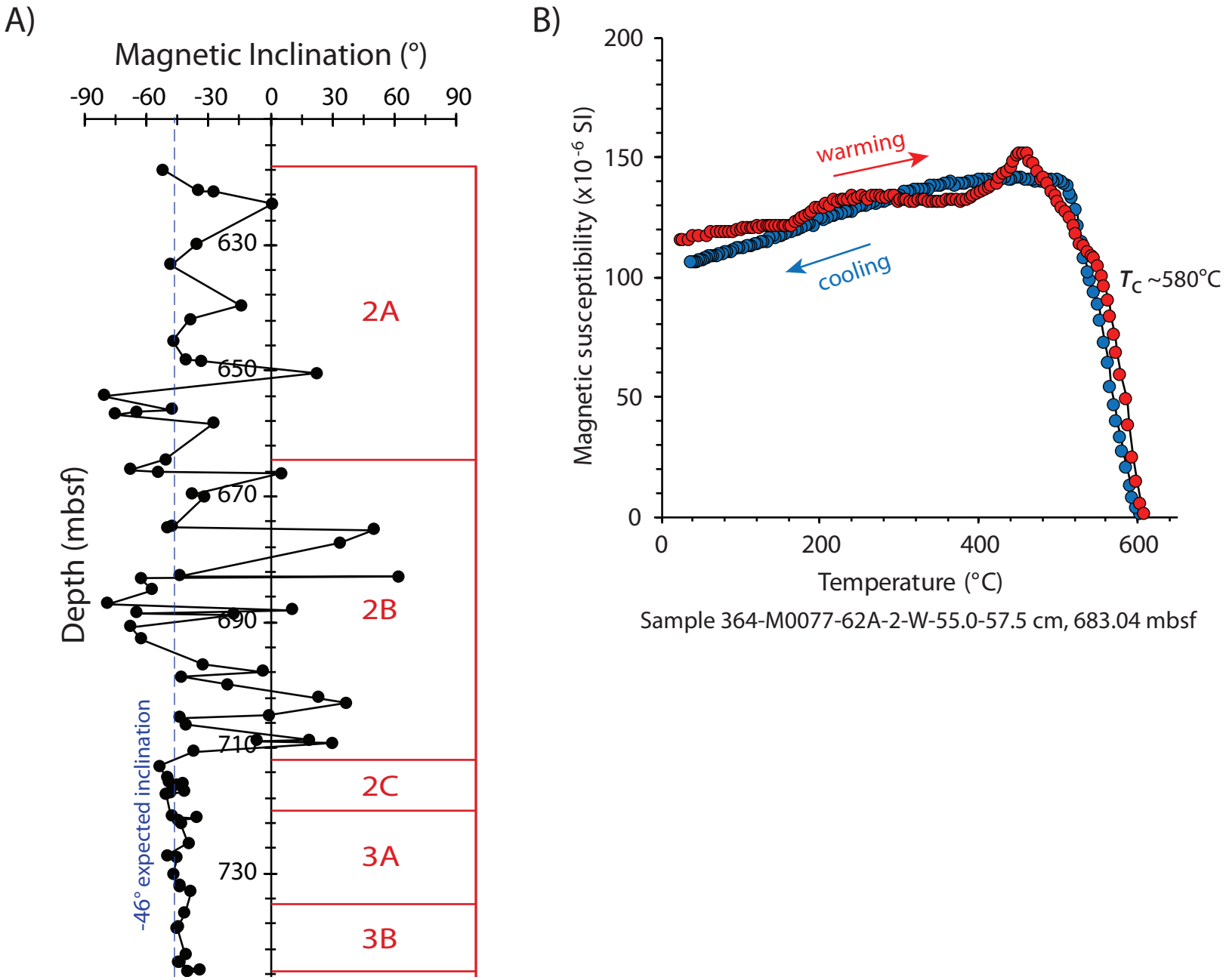
A)
Magnetic Inclination (°)
-90
-60
-30
0
30
60
90
Depth (mbsf)
630
650
670
690
710
730
2A
2B
2C
3A
3B
-46° expected inclination
B)
Magnetic susceptibility (x10-6 SI)
200
150
100
50
0
warming
cooling
TC ~580°C
0
200
400
600
Temperature (°C)
Sample 364-M0077-62A-2-W-55.0-57.5 cm, 683.04 mbsf

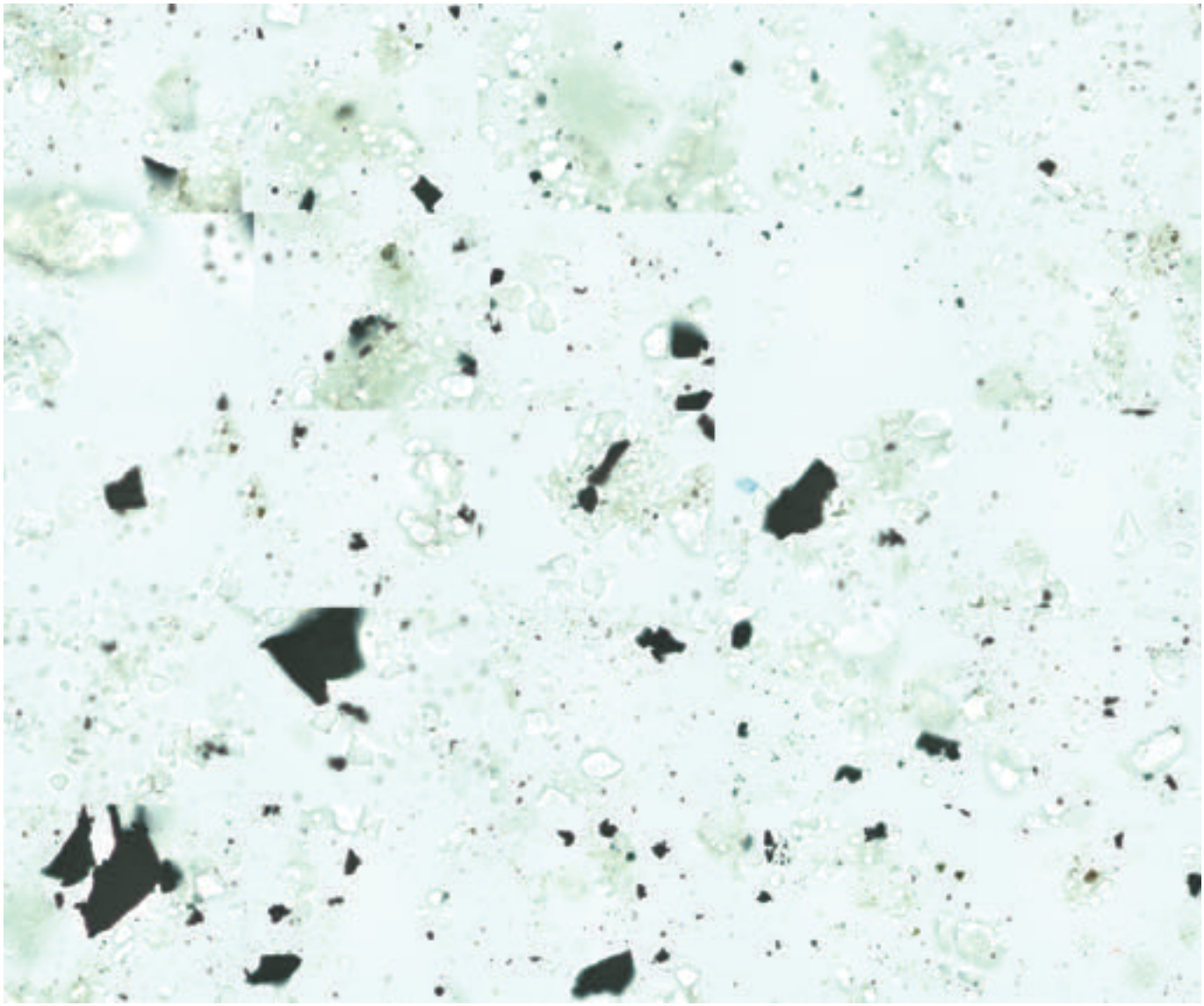

FIGURE S9

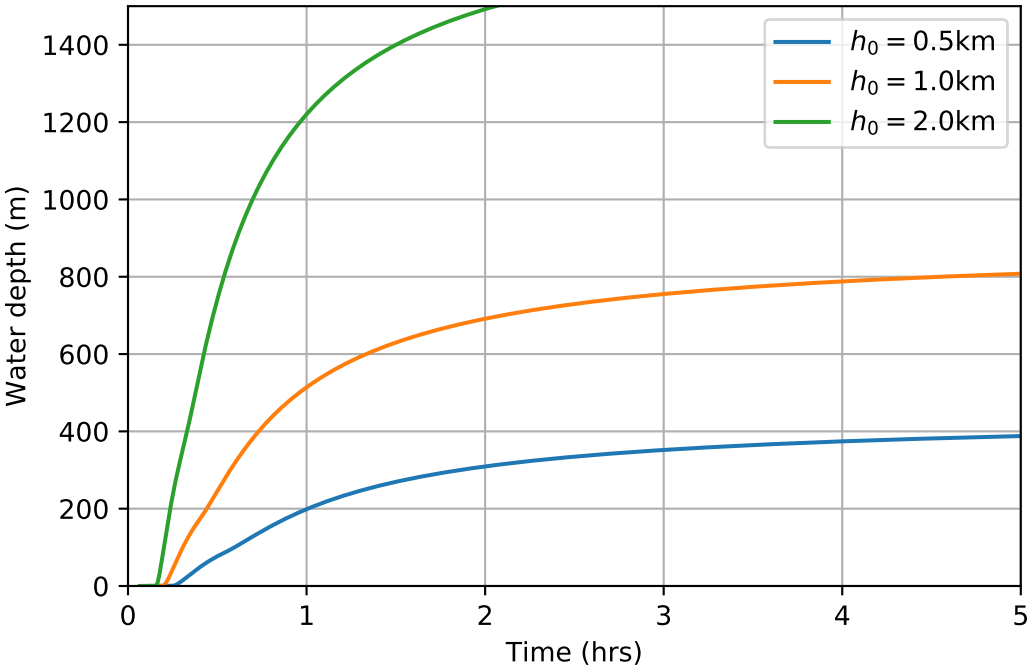
$h_0 = 0.5$km
$h_0 = 1.0$km
$h_0 = 2.0$km
Water depth (m)
Time (hrs)
0
200
400
600
800
1000
1200
1400
0
1
2
3
4
5

FIGURE S10

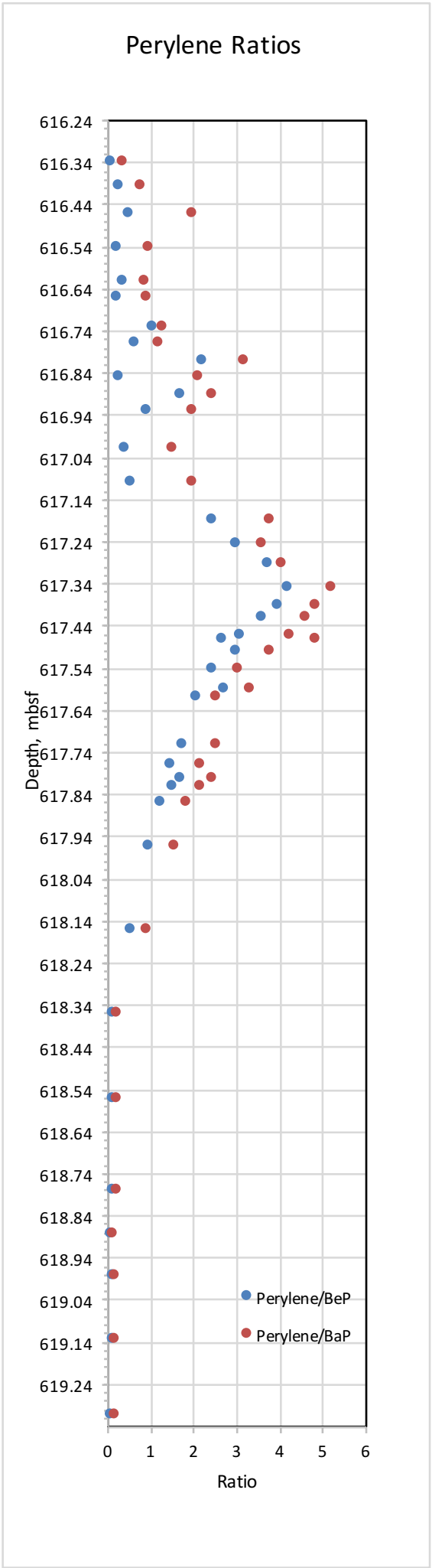
Perylene Ratios
Depth, mbsf
616.24
616.34
616.44
616.54
616.64
616.74
616.84
616.94
617.04
617.14
617.24
617.34
617.44
617.54
617.64
617.74
617.84
617.94
618.04
618.14
618.24
618.34
618.44
618.54
618.64
618.74
618.84
618.94
619.04
619.14
619.24
0
1
2
3
4
5
6
Ratio
Perylene/BeP
Perylene/BaP